eprints@whiterose.ac.uk
https://eprints.whiterose.ac.uk/

Superparamagnetic Graphene Quantum Dot as a Dual-Modality Contrast Agent for Confocal Fluorescence Microscopy and Magnetomotive OCT

Wei Li [1], Wenxing Song [2], Biqiong Chen [3] and Stephen J Matcher[1,*]

[1] Department of Electronic and Electrical Engineering, The University of Sheffield, Sheffield, UK
[2] Department of Chemical and Biological Engineering, The University of Sheffield, Sheffield, UK
[3] School of Mechanical and Aerospace Engineering, Queen's University Belfast, Belfast, UK

*Correspondence:
Stephen J Matcher, Department of Electronic and Electrical Engineering, The University of Sheffield, Broad Lane, S3 7HQ and Sheffield, UK
E-mail: s.j.matcher@sheffield.ac.uk

A magnetic graphene quantum dot (MGQD) nanoparticle, synthesized by hydrothermally reducing and cutting graphene oxide-iron oxide sheet, was demonstrated to possess the capabilities of simultaneous confocal fluorescence and magnetomotive OCT imaging. This MGQD shows low toxicity, significant tunable blue fluorescence and superparamagnetism, which can thus be used as a dual-modality contrast agent for confocal fluorescence microscopy (CFM) and magnetomotive OCT (MMOCT). The feasibility of applying MGQD as a tracer of cells is shown by imaging and visualizing MGQD labelled cells using CFM and our in-house MMOCT. Since MMOCT and CFM can offer anatomical structure and intracellular details respectively, the MGQD for cell tracking could provide a more comprehensive diagnosis.

Location Amplitude Map

1 INTRODUCTION

Cell therapy, which utilizes human or animal cells as therapeutic entities, has been regarded as a new revolution in medicine [1, 2]. It is being rapidly developed to treat diseases such as traumatic brain injury [3], ischaemic heart disease [4], stroke [5], diabetes [6] and limbal epithelial stem cell deficiency (LESCD) [7]. A major challenge for cell therapy is evaluation or comparison of therapy outcomes to determine the best cell type, route, site of transfer, dose, frequency etc. A variety of non-invasive imaging techniques for tracking transplanted cells in vivo have been developed to address the challenge. The main imaging technologies developed for tracking cells are radionuclide, X-ray computed tomography (CT), magnetic resonance imaging (MRI) and optical imaging [8-11].

Each imaging technique has own advantages and limitations. Radionuclide imaging techniques, such as single photon emission computed tomography (SPECT) and positron emission tomography (PET), visualize cells labelled with radioactive isotopes. These have excellent sensitivity, but their application has been limited by the radiation damage, short half-life of tracer and lack of anatomical information [12, 13]. CT can obtain anatomical images with spatial resolution of around 50μm, using heavy element materials, such as gold and bismuth, for cell tracking; hence concerns over

the toxicity of the contrast agent have been raised [14, 15]. Another limitation of CT is that X-ray exposure may result in a risk of cancer and other damage tissue [16]. MRI possesses good spatial resolution (10-100 μm) [14]. The most common tracer for MRI is superparamagnetic iron oxide (SPIO) nanoparticles, which has been clinically approved because of the good biocompatibility [17, 18]. The main disadvantages of MRI are low sensitivity and long acquisition time [13]. High concentrations of magnetic nanoparticles in cells are required for tagging cells due to the low sensitivity [19].

Compared with other image techniques, optical imaging microscopies, such as wide-field microscopy, confocal microscopy (CM), multi-photon laser scanning microscopy and optical coherence tomography (OCT) have a lot of advantages, including cellular level resolution, high sensitivity, strong molecular specificity and non-ionizing radiation [20, 21]. These optical imaging microscopies have been widely applied for molecular and cell biology, due to the excellent resolution [20]. However, optical imaging has limited signal penetration depth due to scattering and absorption of light in tissue. For example, confocal microscopy and multiphoton microscopy provide imaging depth of 200μm and 500μm respectively [22], while OCT can image to 1-2 mm depth, albeit with worse resolution (10μm) [22]. As OCT can provide considerable imaging depth and good enough resolution to easily differentiate tissue structure, it has been clinically used for providing anatomical morphology of tissue in ophthalmology, cardiology and urology [22, 23]. In addition, OCT has features for low cost, portable system, high acquisition rate and easy integration into catheters, hand-held probes or needles; these features let OCT be ideal

for intraoperative imaging [22]. Limitations of OCT include a lack of sub-cellular resolution and insensitivity to fluorescence emission.

Therefore, a contrast agent which could be utilized for diverse imaging modalities would offer more comprehensive information. In this paper, a contrast agent for combined OCT and CM will be described, as it has the potential to provide both anatomical information and valuable intracellular details.

OCT is an optical analog of ultrasound imaging, in which the depth-resolved backscatter from a sample is measured from photon time-of-flight information, recorded indirectly using low-coherence interferometry [24]. The technique was originally implemented in the time-domain, but modern systems almost exclusively use Fourier-domain processing. Fourier-domain OCT (FD-OCT) does not require a mechanically scanned reference arm, allowing higher A-scan rates than TD-OCT. It has been shown that FD-OCT has a >100-fold increase in sensitivity compared with TD-OCT [25].

Similar to CM, the lateral resolution of OCT is limited by the NA of objective, which is defined as $\Delta x = 0.61\lambda/NA$, where λ is the wavelength of light [26]. However, the axial resolution of OCT is determined by the coherence length of the light source. The light source with lower coherence length will produce better axial resolution, expressed as $\Delta z = I_c/2 \cong 0.44\lambda^2/\Delta\lambda$, where $\Delta\lambda$ is bandwidth of light and I_c is the coherence length of light [26]. Because the axial resolution of OCT can be improved by using lower coherence laser source, instead of increase of NA, OCT commonly uses low NA objective for long work distance, deeper imaging depth and a large

FOV. In OCT, specimen is usually illuminated using near-infrared light, because most tissues have a good transparency at near-infrared wavelengths [24, 27].

Since the invention of OCT, various materials have been studied as potential contrast agent. The most common contrast agent is gold nanoparticles with various shapes, involving nanospheres, nanoshells, nanorods, nanocages etc., which is attributed to its surface plasmon resonance effect causing strong size-dependent absorption or scattering at near-infrared wavelengths [24, 28]. Since the development of Spectroscopic OCT, dyes which have a strong absorption or scattering peak in the OCT spectral window also become an important contrast agent, such as indocyanine green and fluorescent microspheres [29, 30]. An approach of locating magnetic particles within tissue using magnetomotive OCT (MMOCT) has been investigated for tracking magnetically labelled cells [31]. In this case, superparamagnetic iron oxide (SPIO) has become the most prevalent contrast agent because of its high magnetic susceptibility, good biocompatibility and easy preparation. It has been reported that ultralow concentrations of SPIO (27 µg/g) within tissue can be detected by MMOCT [32]. The combination of SPIO and MMOCT has been used to track macrophage and platelet, and diagnose breast cancer, atherosclerosis and thrombosis [24, 33-35].

Cell tracking by fluorescence microscopy relies on fluorescence tags to label and locate cells. Most fluorescence probes are either organic fluorophores or quantum dots (QDs). Research work on the quantum dot has been pursued, because organic fluorophores suffer photobleaching and broad overlapping emission lines [10]. QDs are nano-scale nanocrystals, which shows robust fluorescence due to quantum

confinement effect. QDs have many advantages over organic fluorophores, including size-tunable light emission, broad excitation spectra with narrow emission spectra and 20 times brighter and 100 times more stable fluorescence [36, 37]. In earlier research, QDs composed of II–VI (e.g., CdSe, CdS, CdTe) or III–V (e.g., InP, InAs) alloys were developed for their excellent fluorescence [38-40]. However, the applications of these QDs in medicine have been limited by the potential toxicity from heavy metals [41]. QDs based on carbon (e.g., carbon nanotubes, graphene) and silicon (e.g., porous silicon nanoparticles) have been investigated to avoid usage of heavy metal; the results demonstrate that carbon or silicon based QDs have high biocompatibility and efficient fluorescence, thereby, facilitating biomedical applications [41, 42].

The benefits of QDs and SPIO for contrast agents have inspired us to investigate a hybrid QDs and SPIO combination for confocal fluorescence microscopy (CFM) and MMOCT. A recent study shows that a hybrid of graphene and iron oxides, called magnetic graphene quantum dots (MGQD), displays both fluorescence and superparamagnetism [43]. Its properties allow one to integrate CFM and MMOCT in application of cell tracking, thereby possibly simultaneously offering anatomic structure and intercellular details for tissue. In this study, the feasibility of using synthesized MQGD as a contrast agent for MMOCT and CFM will be evaluated.

2 MATERIALS AND METHODS

2.1 Synthesis of MGQD

MGQD nanoparticles were synthesized following a previously reported method [43], with some modifications. First, graphene oxide was prepared from graphite by a modified Hummers method [44]. 0.2 g of graphene oxide was then added into 30 mL of distilled water, dispersed by sonication (60Hz) for 1 hour. The pH value of the suspension was adjusted to 10 by addition of ammonium hydroxide (NH_4OH). 0.8 g of ferric chloride hexahydrate ($FeCl_3$-$6H_2O$, 97%) and 1.04 g of ferrous chloride tetrahydrate ($FeCl_2$-$4H_2O$, >99%) were dissolved into 27 mL distilled water. The ferric salt solution and graphene oxide suspension were mixed up, and NH_4OH was added dropwise until the pH value reached 10. The mixture was stirred for 2 hours under nitrogen atmosphere, forming graphene oxide-iron oxide. The precipitate was then centrifuged and washed several times by water and ethanol until the supernatant became clear, to eliminate uncoated graphene oxide and ions. The graphene oxide-iron oxide was dispersed in 500 mL distilled water and autoclaved by a Parr Series 4000 autoclave at 200 °C for 10 hours, forming shattered reduced graphene oxide-iron oxide nanoparticles, namely MGQD. Then, residual chemicals in the MGQD suspension were removed by dialysis using Fisher Scientific Biodesign Dialysis tubing (molecular weight cut off = 3.5kDa). Finally, the MGQD was dried by freeze drying for storage. All chemicals used above were purchased from Sigma-Aldrich.

2.2 Characterization of MGQD

Transmission electron microscopy (TEM) image of MGQD was achieved using FEI tecnai Biotwin 120 kV machine, operating at accelerating voltage of 80 kV. The electron was emitted by a tungsten filament, and images were recorded on a Gatan Orius SC1000B bottom mounted camera with Gatan Digital Micrograph Software.

TEM sample was prepared by evaporating 10 µL diluted suspension (about 0.01mg/mL) on a carbon film on 200 mesh copper grids. Magnetic hysteresis loop of MGQD was measured by Quantum Design MPMS-XL 5 superconducting quantum interference device (SQUID). 0.016 g of MGQD powder was placed in SQUID, operating with a magnetic field between +20,000Oe and -20,000Oe at 37°C. Magnetic hysteresis loop of SPIO was measured as a control. Fluorescence spectra of MGQD were detected using PerkinElmer LS 55 fluorescence spectrometer. The samples of fluorescence spectrometer were prepared by diluting suspension to about 0.02 mg/mL.

2.3 Cell Culture and Labelling

Cell culture media were prepared by mixing 219mL DMEM+Glutamax (Sigma, D0819), 219mL Ham's F12 (Sigma, N4888), 50mL fetal calf serum (Sigma, F9665), 5mL Penicillin (Sigma, P0781), 5mL Fungizone (Sigma, A2942), 2.5mL insulin (Sigma, 91077C) and 0.025ml EGF (Sigma, E5036). 3T3 cells (derivation of the 3T3 mouse fibroblast cell line) were cultured by adding 2.5×10^5 cells and the 10 mL of medium into a T75 cell culture flask and putting the cell culture flask into incubator until the cells attach and spread out on the bottom. During this time, the medium was renewed once every two days.

A series of concentration (0-100 µg/mL) of MGQD media were prepared by ultrasonically dispersing dried MGQD into media. After cell culture was completed, MGQD media were used to replace the original cell media for cell labelling. These cells and MGQD media were put into an incubator for one day. Then, the labelled cells were washed with PBS 5 times. 2.5 mL of trypsin-EDTA was dropped into flask

to make the cells detach flask. The solution of trypsin-EDTA and cells was added into 7.5 mL medium. The cells in the solution were separated by spinning at 1000 RPM for 5mins. 2 mL medium was added to the separated cells, and the number of cells was calculated by a hemocytometer.

2.4 Toxicity Test by MTT

3T3 cells were seeded into 96-well plates containing 200 µl of RPMI medium (Lonza, BE12-918F) supplemented with 10 % Foetal Bovine Serum (Thermo Fisher, 10500064), 1 % Penicillin-Streptomycin (Lonza, DE17-603E) and 1 % L-Glutamine (Lonza, 17-605F)). The cell seeding density was 5×10^3 cells per well and the cells were incubated overnight at 37 °C under 5% CO_2 atmosphere. Then, the cells were washed twice using PBS buffer and incubated with 200 µl of medium with various concentrations of MGQD. After 24 hours and 48 hours, 50 µl of 3 mg/ml MTT reagent was added into each well and the cells were incubated for another 3 hours. The supernatants were removed and 200 µL of DMSO was added into each well. The absorbance of each well was measured by a plate reader (FLUOstar galaxy, BMG LABTECH, Germany) using 570 nm wavelength.

2.5 CFM Imaging

Confocal imaging of MGQD powder and MGQD labelled cells was performed with an inverted Zeiss LSM 510 NLO microscope. The microscope is equipped with a 30 mW Ar laser (458, 477, 488, 514 nm), a 1.2 mW 543 nm He/Ne laser, a 5 mW 633 nm HeNe laser and a Coherent Chameleon femto-second pulsed laser (690-1040 nm)

suitable for multiphoton imaging. The MGQD was imaged by two-photon excitation using the Coherent Chameleon femto-second pulsed laser. A META multi-wavelength detector was used to collect emitted light from a particular band.

A small quantity of MGQD powder was placed on a microscope slide for CFM imaging. The MGQD labelled cells have been imaged twice. For the first measurement, MGQD labelled cells were fixed on a glass bottomed dish (Thermo Fisher, 150680) using 3.7% paraformaldehyde (in PBS), and visualized directly using 690 nm exciting light. For the second measurement, the MGQD labelled cells were also fixed on a glass bottomed dish, and the F-actin and nucleus of cells were stained by diluted phalloidin-FITC (0.2 µg/mL) and DAPI (1 µg/mL) respectively for highlighting cell shape. The stained cells were imaged using 4 nW laser power at 488 nm and 0.989 mW laser power at 700 nm. The 488 nm laser was used to excite fluorescence of phalloidin-FITC and images F-actin through a 500-550 nm filter. The two-photon fluorescence of DAPI and MGQD was excited by the 700 nm laser and imaged through a 435-485 nm and a 362-415 nm filter, respectively. A control experiment was conducted by imaging unlabeled cells in the same way. The laser powers used for fluorescence excitation were measured by an optical power meter (PM 400, Thorlabs).

2.6 Construction of MMOCT

An in-house MMOCT system was constructed based on a custom-built ultrahigh resolution spectral domain OCT system, shown in Figure 1. A dual super luminescent diode source (Broadlighter D890-HP, Superlum) with 890 nm center wavelength and

150 nm bandwidth was used as the light source. The source bean was split into reference and sample beams by a 50/50 coupler. The sample beam was deflected by a pair of galvanometer scanners (TSH 22556-Y and TSH 22555-X) and focused on a sample by a focus lens (Thorlabs, LSM02-BB) with effective focal length of 17.93 mm and spot size of 9 μm. The galvanometer scanners allow the sample beam to achieve a volumetric scan of a sample. The reference beam was reflected by a plane mirror in reference arm. A variable neutral density filter was placed into the reference arm for attenuating the reference beam. The sample and reference beams were recombined at the 50/50 coupler and propagate to an in-house spectrometer. As the optical path difference between the reference and sample beams is less than coherence length of light source, the interference of reference and sample beams was detected by the spectrometer. An A-scan was obtained by Fast Fourier Transform of the interference pattern, and 500 A-scans were used to construct a B-scan forming an image of width 2 mm. The A-scan acquisition rate was 1000 Hz. The axial and lateral resolutions of this system reached 2.5 μm and 8.8 μm respectively, and the sensitivity was 92 dB.

A homemade electromagnet, an amplifier (7224 DC-Enabled AC Amplifier, AE TECHRON) and a function generator (TENMA 72-6805) were introduced to the OCT system to generate sinusoidal magnetic field. Sample was exposed to the magnetic field when image was acquired.
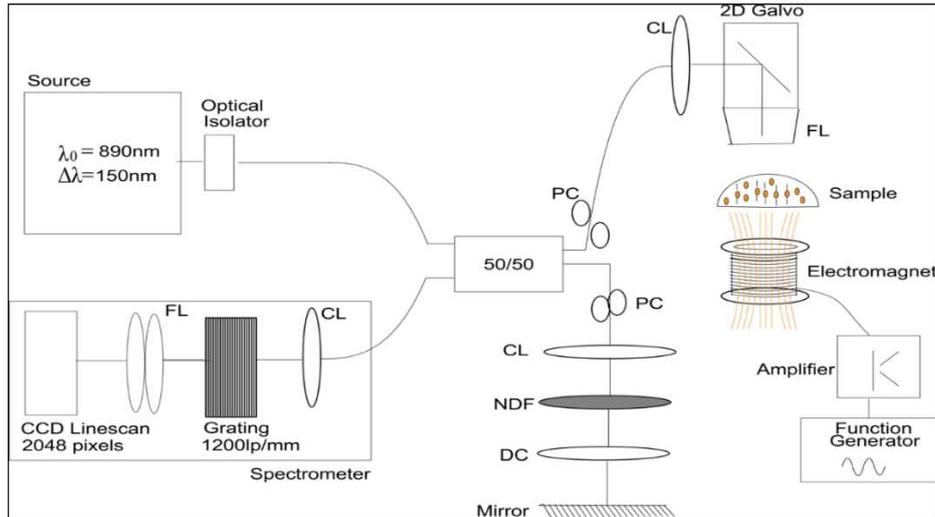
FIGURE 1. The schematic of custom-built MMOCT system, where PC is polarization controller, CL is calibrating collimator, FL is focus lens DC is dispersion compensator and NDF is neutral density filter. A dual super luminescent diode source (Broadlighter D890-HP, Superlum) emitting 890nm of light with a bandwidth of 150 nm was used. The emitted beam passed through an optical fiber isolator (IO-F-SLD150-895, Thorlabs), and then was split into sample arm and reference arm by 50/50 coupler (Nufern 630-HP fiber, Gould Fiber Optics). The sample beam passed through a polarization controller (PolaRITETM, General Photonics) and a collimator (PAF-X-5-B, ThorLabs) before being deflected by galvo-mounted mirrors, and focused by a telecentric OCT scan lens (LSM02-BB, Thorlabs). The reference beam passed through a collimator (PAF-X-5-B, ThorLabs) and a dispersion compensator (LSM02DC, Thorlabs) before being reflected by a fixed plane mirror, and its intensity was adjusted by an adjustable neutral density filter. The spectrometer in this system for detecting recombined sample and reference beams was made up of a 1200-line pair per mm diffraction grating (Wasatch Photonics, Inc.) and 2048 pixel line scan camera (Aviiva, EV71yEM1GE2014-BA9, e2v). A homemade electromagnet, a functional generator (TENMA 72-6805) and an amplifier (7224 DC-Enabled AC Amplifier, AE TECHRON) were introduced to generate a sinusoidal magnetic field at 80Hz for inducing magnetomotive signal of sample.

2.7 MMOCT imaging

Since agar gel has shown similar mechanical properties to soft tissue [45], agar was used to mimic human soft tissue in this experiment. The agar gel was prepared by shaking and microwave heating of 10 g/L agar solution. As one of our clinical application areas is tracking transplanted corneal stem cells [46], MGQD labelled cells were deposited on the surface of agar gel for acquisition of MMOCT image.

The MMOCT samples were placed over electromagnet, 1 cm away from the top of the electromagnet, in an 80-Hz sinusoidal magnetic field with strength of 0.05 T. The scanning scheme for MMOCT imaging was implemented by a successively scanning along the transverse dimension with a high degree of spatial oversampling and temporal oversampling, which must satisfy the following condition:

$$f_z > 2f_B > \frac{2v}{\Delta x} \tag{1}$$

where f_z is the axial line acquisition rate, f_B is the magnet modulation frequency, Δx is transverse resolution and v is transverse scan velocity [32]. In the experiment, an axial acquisition rate of 1 kHz and 5000 A-scans for 2 mm scan distance were applied, resulting in the transverse scan velocity v of 0.4 mm/s. 80 Hz magnetic modulation frequency were chosen to meet the condition (1). The phase of each A-scan was unwrapped and spatially localized frequency spectrum of the phase change was computed by a Short Time Fourier Transform (STFT). The magnetomotive signal of paramagnetic nanoparticles appears at twice the field modulation frequency i.e. 160 Hz (or its harmonics) and was thus extracted by a band-pass filter centered on 160 Hz (or harmonic). The STFT window length was 50 points, corresponding to a lateral resolution of 20μm.

3. RESULTS AND DISCUSSION

3.1 MGQD Structure

The morphology of synthesized MGQD has been investigated by TEM, shown in Figure 2. The MQGD is approximately a round thin sheet with around 15 nm of average diameter. The diameter of this MGQD is smaller than that of the MGQD

reported by Justin et al [43], presumably because of the different graphene oxide

powders and conditions used for synthesizing the MGQDs. Compared with other

popular nanoparticles for cell labelling, e.g. standard SPIO (with a diameter of 50-150

nm) [47] and commercial gold nanoparticles (with a diameter of 30-90 nm)[48], the

size of MGQD is relatively small. The small size could benefit MGQD uptake, since

nanoparticles with small size could require less surface energy creation during the

cellar internalization process [49]. In Figure 2, it is expected that the light gray areas

are uncovered graphene, while the dark gray regions result from iron oxide coated

graphene. Hence the TEM suggests that the distributions of size, shape and coating
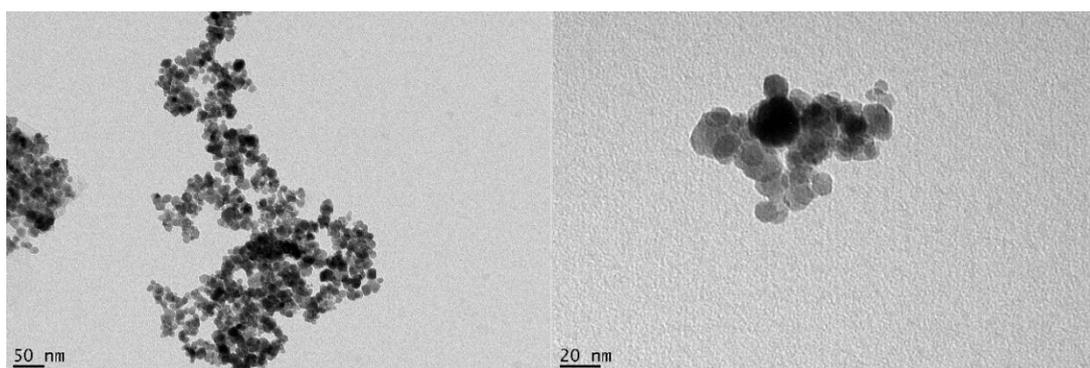
area of iron oxides is uneven.

FIGURE 2. TEM images of MGQDs with magnification of 30000 (left) and 98000 (right),
where the light black and dark black areas could be uncovered graphene and iron oxides
coated graphene respectively.

3.2 Magnetism of MGQD

The iron oxides on graphene were synthesized from co-precipitation of ferrous and

ferric ions under alkaline condition, which can be exemplified by $Fe^{2+} + 2Fe^{3+} +$

$8OH^- \rightarrow Fe_3O_4$ (magnetite) $+4H_2O$ [43]. This results in graphene oxide particles coated

with magnetite. A hydrothermal reaction is then used to cut these particles, yielding

nanometre-scale MGQD. The hydrothermal cutting also oxidize a fraction of the magnetite, transforming it into maghemite (γFe_2O_3) [50]. Therefore, the iron oxides containing a mixture of magnetite and maghemite were produced on the graphene surface [43]. The iron oxides can provide strong superparamagnetism for MMOCT imaging. To quantify the magnetic properties, the magnetic hysteresis curve of MGQD was measured using a SQUID magnetometer, and commercial SPIO nanoparticles (Sigma-Aldrich) which have been widely used as an MMOCT contrast agent was also measured for comparison. Both results are shown in Figure 3a. The saturation magnetization of MGQD is 41.7emu/g, higher than the MGQD reported previously (7.31 emu/g) [43]. We have observed that preventing oxidation of Fe^{2+} by atmospheric oxygen both during the preparation of the ferrous iron solution and during the co-precipitation of magnetite can increase the saturation magnetization of MGQD significantly. We perform both of these steps under a 100% nitrogen atmosphere, which thus could explain our higher saturation magnetization. The absence of coercivity revealed in the magnetic hysteresis curves of MGQD and SPIO shows that both MGQD and SPIO are superparamagnetic, and hence suitable for tracer agents in MMOCT.

As the magnetomotive contrast in MMOCT is generated by an oscillation of magnetic nanoparticles in an alternating magnetic field, a relatively high magnetic susceptibility of nanoparticle is required for inducing sufficient translational force. The translational force (F) can be defined as:

$$\vec{F} = \frac{V(\chi_m - \chi_0)\nabla|\vec{B}|^2}{2\mu_0} \tag{2}$$

where V is the particle volume, χ_m and χ_0 are the magnetic susceptibilities of the particle and the tissue respectively, B is magnetic flux density and μ_0 is the

permeability of free space[31]. The (bulk) magnetic susceptibilities (χ) and

magnetization (M) are related by the following relationship:

$$M = \chi H \tag{3}$$

where H is the magnetic field strength. The the magnetic susceptibilities of MGQD

and SPIO have been plotted in Figure 3b. As expected, MGQD has lower

magnetization and magnetic susceptibility than SPIO, since the mass ratio of iron

oxides in MGQD is less than SPIO's. The magnetic susceptibility of MGQDs are

comparable to SPIO's in magnetic field of 100-10000 Oe, and is much higher than

human tissue ($|\chi| \sim 10^{-5}$) [31]. Hence, MGQD could offer reliable performance as a
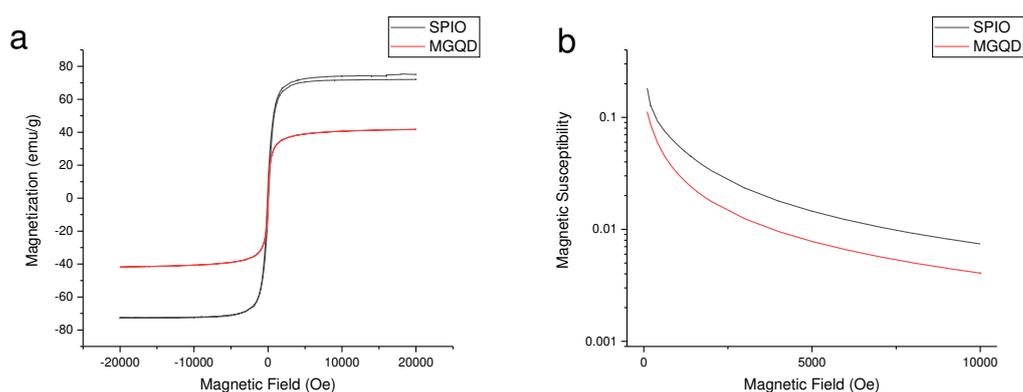
contrast agent for MMOCT.

FIGURE 3. a: the magnetic hysteresis curves of MGQD and SPIO; the MGQD and SPIO have 41.7emu/g and 75.2emu/g of saturation magnetization respectively. **b**: the magnetic susceptibilities of MGQD and SPIO in magnetic field of 100-10000 Oe; magnetic susceptibilities of MGQD and SPIO decrease with increasing magnetic field strength; at the lowest field strength (100 Oe), the magnetic susceptibilities of MGQD and SPIO are 0.112 and 0.182 respectively; the magnetic susceptibilities of MGQD and SPIO are 0.027 and 0.050 respectively at the highest field strength (1200 Oe).

3.3 Fluorescence of MGQD

Pan et al (2010) have synthesized a carbon-based material, graphene quantum dot

(GQD), which has a strong $\pi \rightarrow \pi^*$ absorption peak at 320 nm and a blue

photoluminescence or fluorescence at 430 nm [51]. The GQD was formed by

hydrothermal reduction of graphene oxide at 200℃. It is expected that MGQD has the

similar blue fluorescence because MGQD was synthesized by reducing and cleaving

iron oxide-graphene oxide sheets in the same way. The fluorescence of MGQD has

been investigated by a fluorescence spectrometer to initially assess whether the

synthesized MGQD can be used as tracer in fluorescence microscope, shown in

Figure 4. As with GQD [51], an absorption peak at 320 nm is also be observed for the

MGQD. However, the excitation peak becomes 360 nm rather than 430 nm due to

effect of the coated iron oxides and change of particle size. Our 360 nm excitation

peak is also different from the MGQD synthesized previously (excitation peak 398

nm) [43]. This might be because of the smaller size of our MGQD, which is expected

to yield a larger band gap due to enhanced quantum confinement of the electrons [52].

The peak emission intensity of MGQD can be tuned by tuning the excitation

wavelength, shown in Figure 4b, which is the same as GQD synthesized by Pan et al

[51]. Visible fluorescence with a peak at 415 nm was excited using 360 nm excitation.

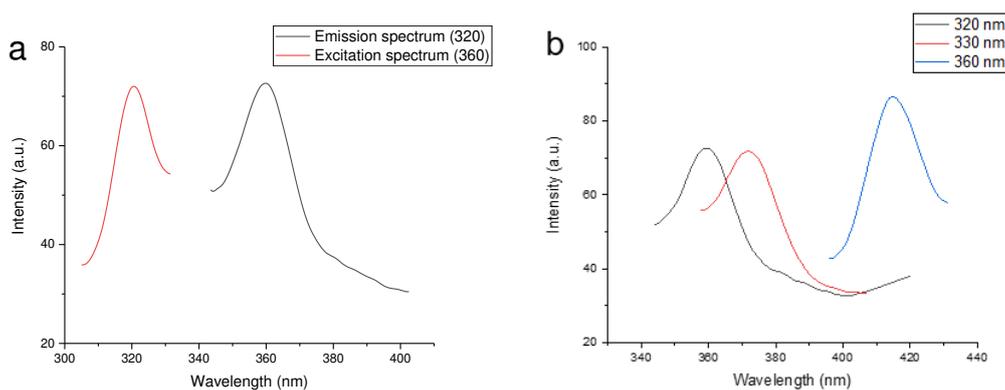Therefore, the MGQDs have the potential to be contrast agent for CFM.

FIGURE 4. Fluorescence spectra of MGQDs. **a**: The excitation wavelength versus emission wavelength, where the emission spectrum excited by 320nm of light is shown as "Emission spectrum (320)", and the excitation spectrum of MGQD measured by a fixed wavelength at 360 nm is shown as "Excitation spectrum (360)". **b**: The emission spectrums of MGQDs excited by 320 nm, 330 nm and 360 nm respectively, showing excitation-dependent fluorescence behaviors of MGQDs.

3.4 Toxicity of MGQD

It is essential that nanoparticles for cell labelling have very low toxicity for cells. Hence, the effect of MGQD on 3T3 cell line has been tested by MTT method, shown in Figure 5. The 3T3 cells in the media containing 0-104 μg/mL MGQDs retain more than 87% cell viability at 24 and 48 hours' incubation times. In contrast, SPIO nanoparticles (100 μg/mL) which have been widely applied as a contrast agent for MRI show a cell viability of 80% after 24 hours culture [53]. Therefore, MGQDs in concentration below 104 μg/mL display extremely low cytotoxic effects to 3T3 cells. For MMOCT and CFM imaging, the 3T3 cells were labelled by 24-hour culturing in medium containing MGQD in the concentration below 104 μg/mL, so MGQD is considered as a safe contrast agent for MMOCT and CFM.
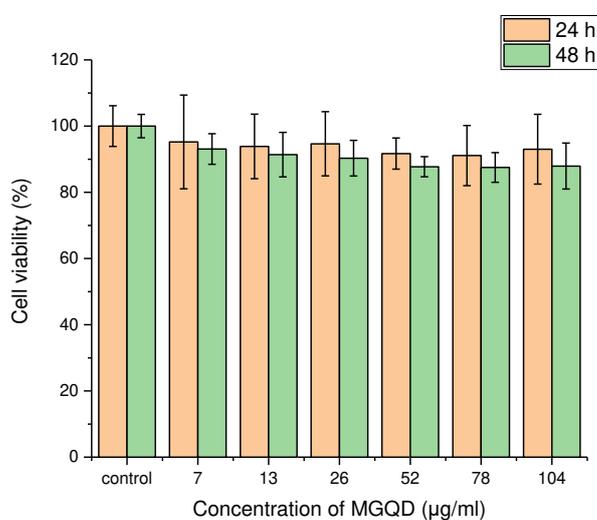

FIGURE 5. The influence of MGQD in concentrations of 7, 13, 26, 52, 78 and 104 μg/mL on cell line viability of 3T3 cell line after 24 and 48 hours culture.

3.5 CFM imaging of MGQD

It has been shown that MGQD exhibits tunable fluorescent behavior within the exciting wavelength range of 320-360nm. Hence, two-photon fluorescence of MGQD should be excitable by a laser with wavelength around 700 nm. The fluorescence of MGQD powder has been imaged by CFM using 740 nm excitation light, shown in Figure 6a. A blue fluorescence signal was detected in the wavelength range 435-485 nm. The 3T3 cells labelled by incubation in 75 μg/mL MGQD medium for 24 hours have been visualized through CFM using 690 nm excitation light, shown in Figure 6b. The MGQD is internalized into cells and can be recognized by its fluorescence signal in the CFM image. However, some aggregation of MGQD occurs and thereby inhibit a portion of fluorescence. The aggregation effect could be a limitation of MGQD for CFM application, as MGQD tends to aggregate at high concentration, possibly due to the presence of weak remnant magnetization. It should also be noted that these MGQD's have not been steric stabilized e.g. by PEGylation. In Figure 6c, the 3T3 cells labelled by 15 μg/mL MGQD medium are imaged using 700 nm exciting light, where the cell nucleus (in red) and actin (in green) were stained by DAPI and phalloidin-FITC respectively. The fluorescence signal of MGQD is observed within the cell nucleus and also attached to actin filaments in the range of 362-415 nm wavelength and highlighted in blue in Figure 6c. There is no specific region where MGQD tends to aggregate. Figure 6d is the CFM image of unlabeled cells for negative control, in which blue fluorescence signal is not evident.
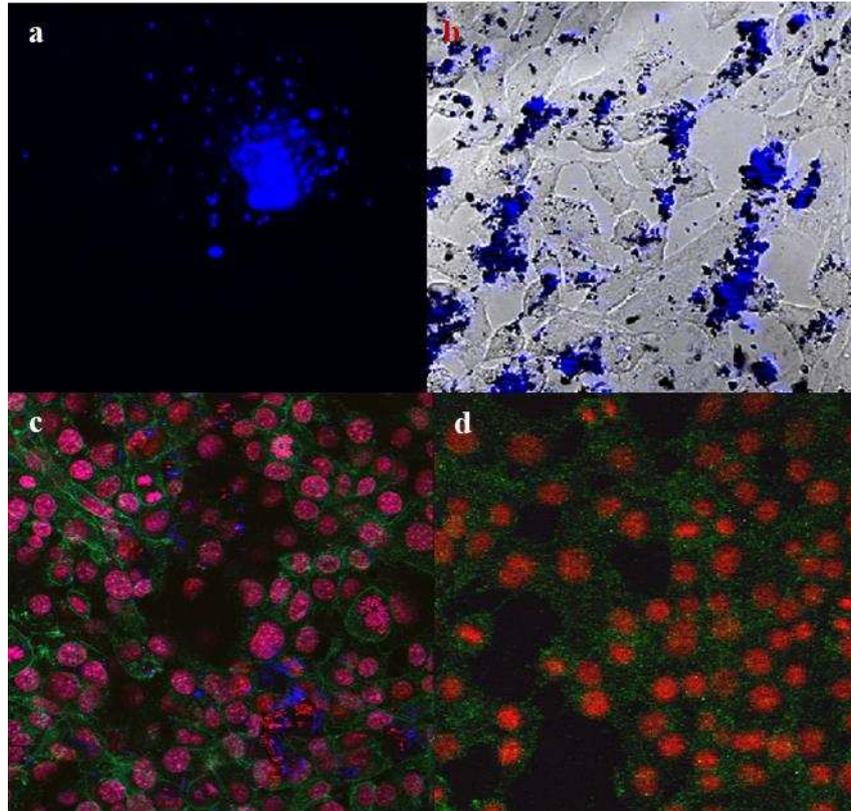
FIGURE 6. The CFM images of MGQD powder and MGQD labelled cells, where MGQD, cell nucleus and actin are shown in blue, red and green respectively. **a**: MGQD powder (×40 magnification, 1.2 NA) imaged using 3.75 mW 740 nm excitation light and 390-465 nm emission filter; **b**: 75 μg/mL MGQD labelled 3T3 cells (×20 magnification, 0.8 NA) imaged using 14.35 mW 690 nm excitation light and 543 nm transmission light, where the fluorescence of MGQD is obtained by 362-415 nm filter; **c**: 15 μg/mL MGQD labelled 3T3 cells (×40 magnification, 1.2 NA) imaged using 0.989 mW 700 nm and 4 nW 488 nm excitation lights, where the MGQD and DAPI are excited with 700 nm light, phalloidin-FITC is excited with 488 nm light and 362-415 nm, 435-485 nm and 500-550 nm filters are used to obtain the fluorescence of MGQD, DAPI of cell nucleus and phalloidin-FITC of actin, respectively; **d**: unlabeled 3T3 cells (×20 magnification, 0.8 NA) imaged using the same excitation lights and emission filters as **c** for comparison.

3.6 MMOCT imaging of MGQD

MGQD labelled 3T3 cells are loaded on surface of agar gel for MMOCT imaging, where the agar gel is utilized to mimic human soft tissue. An 80 Hz sinusoidal magnetic field generated by an electromagnet is applied for exerting force on MGQD and generating magnetomotive signal of MGQD. The translative force vector of

MGQD ($\vec{F}$) is parallel with the magnetic field vector ($\vec{B}$) and the axial direction of A scan (z), which can be expressed as:

$$\vec{F} = V(M_r + \frac{\chi_m}{\mu_0}B_z)\frac{\partial \vec{B}}{\partial z} \tag{4}$$

where M_r is remnant magnetization. The remnant magnetization is negligible due to the superparamagnetism of MGQD. The magnetomotive force is unidirectional because of the positivity of χ_m and $B_z\frac{\partial \vec{B}}{\partial z}$. Therefore, the oscillation of MGQD should have double the frequency of the magnetic field modulation. The frequency spectrum of 35 μg/mL MGQD labelled cells on agar (density$\approx 1.9 \times 10^5$cell/cm^2) has been detected by MMOCT, shown in Figure 7b. A 320 Hz of magnetomotive signal (intensity$\approx 7.9 \times 10^5$ a.u.) is dominant rather than the expected oscillation frequency of 160 Hz. The second or higher harmonic frequencies could be generated from overlarge amplitude of particle displacement causing phase wrapping. In other words, the displacements of particles within the interval time of two successive samplings is too large, leading to the phase change of interferometric signal greater than π. The dominant magnetomotive signal (320 Hz) is extracted using a bandpass filter for forming image of MGQD labelled cells, shown in Figure 7c. The MGQD labelled cells are visualized successfully, which demonstrates the feasibility of using MGQD as a contrast agent for MMOCT. However, it is apparent that the magnetomotive signal of MGQD can also be detected inside agar gel. This phenomenon could be explained by the MGQD diffusing into the agar gel, by the MGQD on the agar surface forming a shadow artefact beneath surface (similar to the "shower curtain" effect in OCT angiography) or the MGQD inducing a bulk vibration of agar. In Figure 7 d, e and f, the same amount of unlabeled 3T3 cells on agar surface as the negative control are imaged in the same way. No magnetomotive signal is detected for the negative

control, which confirms the magnetomotive signal resulting from oscillation of MGQD.

MGQD has demonstrated effectiveness as an MMOCT tracer, and low concentrations of MGQD can be used to label cells whilst producing identifiable magnetomotive signal. In our experiment, the minimum useable MGQD concentration is 20 μg/mL. Quantitative analyses of MGQD uptake in cells using magnetomotive signal intensity is complicated, because the magnetomotive signal of MGQD is partially redistributed to its higher harmonics. The magnetomotive signal redistribution arises from phase wrapping, which could be prevented by using a higher line scan rate or lower magnetic field strength [54]. Therefore, MGQD has the potential for quantitative measurement of labelled cells.
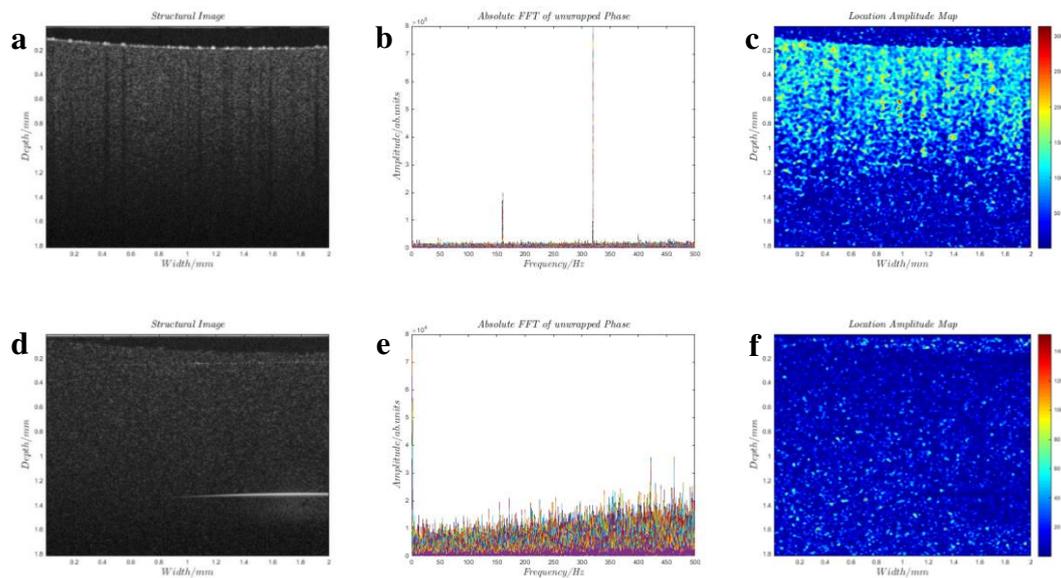

FIGURE 7. The MMOCT images of MGQD labelled 3T3 cells and unlabeled 3T3 cells on agar gel. **a**: the original B-scan OCT image of 35 μg/mL MGQD labelled cells without MMOCT signal processing, where the cell intensity imaged is approximately 1.9×10^5 cell/cm^2; **b**: the phase frequency spectrum of magnetomotive signal of MGQD labelled cells; **c**: the MGQD labelled cells phantom results from MMOCT signal processing of 320 Hz magnetomotive signal; **d**, **e** and **f** are the images and spectrum of unlabeled cells for negative control, which are original B-scan OCT image, phase frequency spectrum and MMOCT image respectively.

4. CONCLUSION

MGQD nanoparticles were synthesized by hydrothermal reduction of iron oxide coated graphene oxide sheets. The MGQD shows up as a small round thin sheet (15 nm of average diameter) with low toxicity to cells, which allows MGQD to be easily internalized into cells for labeling. The iron oxides and graphene of MGQD can offer superparamagnetism and tunable blue fluorescence simultaneously. These properties suggest that MGQD can be used as a dual-modality contrast agent for CFM and MMOCT. The MGQD labeled cells have been successfully tracked and visualized by a commercial CFM and our in-house MMOCT system. Application of MGQD for cell tracking could provide anatomical information via MMOCT and intracellular details via CFM, thereby achieving a more comprehensive diagnosis.

REFERENCES

[1] M. A. Fischbach, J. A. Bluestone, W. A. Lim *Sci. Transl. Med.* **2013**, *5*, 179ps7.
[2] M. R. Bernsen, J. Guenoun, S. T. Van Tiel, G. P. Krestin *The British journal of radiology*. **2015**, *88*, 20150375.
[3] S. Gennai, A. Monsel, Q. Hao, J. Liu, V. Gudapati, E. L. Barbier, J. W. Lee *Br. J. Anaesth.* **2015**, *115*, 203.
[4] J. Tongers, D. W. Losordo, U. Landmesser *Eur. Heart J.* **2011**, *32*, 1197.
[5] Y. Luo *J. Neural Transm.* **2011**, *118*, 61.
[6] C. Aguayo-Mazzucato, S. Bonner-Weir *Nature Reviews Endocrinology*. **2010**, *6*, 139.
[7] A. J. Shortt, S. J. Tuft, J. T. Daniels *Br. Med. Bull.* **2011**, *100*, 209.
[8] M. Srinivas, E. Aarntzen, J. W. M. Bulte, W. J. Oyen, A. Heerschap, I. J. M. De Vries, C. G. Figdor *Adv. Drug Del. Rev.* **2010**, *62*, 1080.
[9] M. Hoehn, D. Wiedermann, C. Justicia, P. Ramos‐Cabrer, K. Kruttwig, T. Farr, U. Himmelreich *The Journal of physiology*. **2007**, *584*, 25.

[10] A. P. Alivisatos, W. Gu, C. Larabell *Annu. Rev. Biomed. Eng.* **2005**, *7*, 55.

[11] A. Astolfo, E. Schültke, R. H. Menk, R. D. Kirch, B. H. J. Juurlink, C. Hall, L.-A. Harsan, M. Stebel, D. Barbetta, G. Tromba *Nanomed. Nanotechnol. Biol. Med.* **2013**, *9*, 284.

[12] A. K. Srivastava, J. W. M. Bulte *Stem Cell Reviews and Reports.* **2014**, *10*, 127.

[13] A. C. O'Farrell, S. D. Shnyder, G. Marston, P. L. Coletta, J. H. Gill *Br. J. Pharmacol.* **2013**, *169*, 719.

[14] R. Weissleder, M. J. Pittet *Nature.* **2008**, *452*, 580.

[15] R. Bayford, T. Rademacher, I. Roitt, S. X. Wang *Physiol. Meas.* **2017**, *38*, R183.

[16] D. M. Mills, S. Tsai, D. R. Meyer, C. Belden *Am. J. Ophthalmol.* **2006**, *142*, 1046.

[17] R. Jin, B. Lin, D. Li, H. Ai *Curr. Opin. Pharmacol.* **2014**, *18*, 18.

[18] A. Taylor, A. Herrmann, D. Moss, V. Sée, K. Davies, S. R. Williams, P. Murray *PLoS One.* **2014**, *9*, e100259.

[19] S. M. Janib, A. S. Moses, J. A. MacKay *Adv. Drug Del. Rev.* **2010**, *62*, 1052.

[20] W. Du, Y. Wang, Q. Luo, B.-F. Liu *Anal. Bioanal. Chem.* **2006**, *386*, 444.

[21] C. Balas *MeScT.* **2009**, *20*, 104020.

[22] N. M. Fried, A. L. Burnett *Nature Reviews Urology.* **2015**, *12*, 451.

[23] J. E. R. de Carvalho, F. D. Verbraak, M. C. Aalders, C. J. van Noorden, R. O. Schlingemann *Surv. Ophthalmol.* **2014**, *59*, 393.

[24] W. Drexler, J. G. Fujimoto, Optical coherence tomography: technology and applications, Springer, **2015**.

[25] N. Nassif, B. Cense, B. H. Park, S. H. Yun, T. C. Chen, B. E. Bouma, G. J. Tearney, J. F. de Boer *OptL.* **2004**, *29*, 480.

[26] P. H. Tomlins, R. K. Wang *Journal of Physics D: Applied Physics.* **2005**, *38*, 2519.

[27] F. F. Jobsis *Science.* **1977**, *198*, 1264.

[28] A. Y. Gordon, A. Jayagopal *Journal of nanomedicine & nanotechnology.* **2014**, 4.

[29] C. Yang, L. E. L. McGuckin, J. D. Simon, M. A. Choma, B. E. Applegate, J. A. Izatt *OptL.* **2004**, *29*, 2016.

[30] J. Yi, J. Gong, X. Li *Opt. Express.* **2009**, *17*, 13157.

[31] A. L. Oldenburg, J. R. Gunther, S. A. Boppart *OptL.* **2005**, *30*, 747.

[32] A. L. Oldenburg, V. Crecea, S. A. Rinne, S. A. Boppart *Opt. Express.* **2008**, *16*, 11525.

[33] J. Oh, M. D. Feldman, J. Kim, H. W. Kang, P. Sanghi, T. E. Milner *Lasers Surg. Med.* **2007**, *39*, 266.

[34] A. L. Oldenburg, C. M. Gallippi, F. Tsui, T. C. Nichols, K. N. Beicker, R. K. Chhetri, D. Spivak, A. Richardson, T. H. Fischer *Biophys. J.* **2010**, *99*, 2374.

[35] R. John, R. Rezaeipoor, S. G. Adie, E. J. Chaney, A. L. Oldenburg, M. Marjanovic, J. P. Haldar, B. P. Sutton, S. A. Boppart *Proceedings of the National Academy of Sciences.* **2010**, *107*, 8085.

[36] I. L. Medintz, H. T. Uyeda, E. R. Goldman, H. Mattoussi *Nature materials.* **2005**, *4*, 435.

[37] W. C. W. Chan, S. Nie *Science.* **1998**, *281*, 2016.

[38] Z. A. Peng, X. Peng *J. Am. Chem. Soc.* **2001**, *123*, 183.

[39] R. Xie, D. Battaglia, X. Peng *J. Am. Chem. Soc.* **2007**, *129*, 15432.

[40] X. Peng, J. Wickham, A. Alivisatos *J. Am. Chem. Soc.* **1998**, *120*, 5343.

[41] A. Das, P. T. Snee *Chemphyschem.* **2016**, *17*, 598.

[42] J.-H. Park, L. Gu, G. Von Maltzahn, E. Ruoslahti, S. N. Bhatia, M. J. Sailor *Nature materials*. **2009**, *8*, 331.

[43] R. Justin, K. Tao, S. Román, D. Chen, Y. Xu, X. Geng, I. M. Ross, R. T. Grant, A. Pearson, G. Zhou *Carbon*. **2016**, *97*, 54.

[44] D. C. Marcano, D. V. Kosynkin, J. M. Berlin, A. Sinitskii, Z. Sun, A. Slesarev, L. B. Alemany, W. Lu, J. M. Tour *ACS nano*. **2010**, *4*, 4806.

[45] G. Lamouche, B. F. Kennedy, K. M. Kennedy, C.-E. Bisaillon, A. Curatolo, G. Campbell, V. Pazos, D. D. Sampson *Biomedical optics express*. **2012**, *3*, 1381.

[46] J. Boadi, V. Sangwal, S. MacNeil, S. J. Matcher in System for tracking transplanted limbal epithelial stem cells in the treatment of corneal stem cell deficiency, Vol. 9328 (Ed.^Eds.: Editor), City, pp.93281D.

[47] D. L. J. Thorek, A. Tsourkas *Biomaterials*. **2008**, *29*, 3583.

[48] D. Mateo, P. Morales, A. Ávalos, A. I. Haza *J. Exp. Nanosci.* **2015**, *10*, 1401.

[49] C. He, Y. Hu, L. Yin, C. Tang, C. Yin *Biomaterials*. **2010**, *31*, 3657.

[50] S. Laurent, D. Forge, M. Port, A. Roch, C. Robic, L. Vander Elst, R. N. Muller *Chem. Rev.* **2008**, *108*, 2064.

[51] D. Pan, J. Zhang, Z. Li, M. Wu *Advanced materials*. **2010**, *22*, 734.

[52] A. P. Alivisatos *Science*. **1996**, *271*, 933.

[53] H.-C. Hsieh, C.-M. Chen, W.-Y. Hsieh, C.-Y. Chen, C.-C. Liu, F.-H. Lin *JNR*. **2015**, *17*, 71.

[54] H. C. Hendargo, M. Zhao, N. Shepherd, J. A. Izatt *Opt. Express*. **2009**, *17*, 5039.